ACS APPLIED ENERGY MATERIALS

www.acsaem.org Article

Thin Thermally Evaporated Organic Hole Transport Layers for Reduced Optical Losses in Substrate-Configuration Perovskite Solar Cells

Benjamin T. Feleki, Christ H. L. Weijtens, Martijn M. Wienk, and René A. J. Janssen*

Cite This: *ACS Appl. Energy Mater.* 2021, 4, 3033−3043 Read Online

ACCESS | Metrics & More | Article Recommendations | Supporting Information

ABSTRACT: Parasitic optical absorption is one of the root causes of the moderate efficiency of metal halide perovskite solar cells (PSCs) with an opaque substrate configuration. Here, we investigate the reduction of these optical losses by using thin (7−10 nm), undoped, thermally evaporated 2,2′,7,7′-tetrakis[*N*,*N*-di(4-methoxyphenyl)amino]-9,9′-spirobifluorene (spiro-OMeTAD), *N*,*N*′-di(1-naphthyl)-*N*,*N*′-diphenyl-(1,1′-biphenyl)-4,4′-diamine) (NPB), and tris(4-carbazoyl-9-ylphenyl)-amine) (TCTA) hole transport layers (HTLs). Of these, NPB is found to offer the best compromise between efficiency and stability. In semitransparent n−i−p configuration PSCs with an indium tin oxide bottom and a MoO_3/thin-Au/ZnS dielectric−metal−dielectric top electrode, NPB gives 14.9% and 10.7% efficiency for bottom and top illumination, respectively. The corresponding substrate-configuration PSC fabricated on an Au bottom electrode has 13.1% efficiency. Compared to a 14.0% efficient PSC with a thick spin-coated doped spiro-OMeTAD layer, the cell with NPB provides an improved short-circuit current density but has slightly lower open-circuit voltage and fill factor. Detailed analysis of the optical losses in the opaque devices demonstrates that evaporated NPB offers negligible parasitic absorption compared to solution-processed spiro-OMeTAD. The optical losses that remain are due to absorption and reflection of the transparent top electrode.

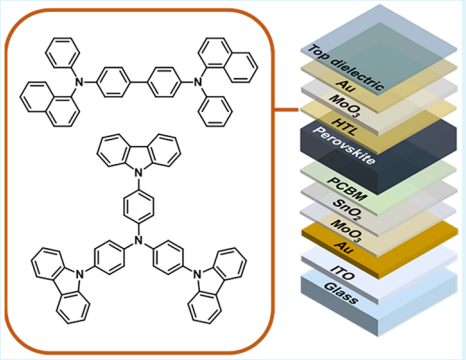

KEYWORDS: *metal halide perovskite, solar cell, hole transport layer, substrate configuration, optical modeling, top illumination*

1. INTRODUCTION

Integrating solar cells into the outer envelope skin of buildings could one day revolutionize how electrical energy is supplied on demand.[1−3] As a promising photovoltaic technology for building-integrated photovoltaics, metal halide perovskite solar cells (PSCs) have recently reached important milestones in both stability and power conversion efficiency (PCE) with a certified 25.2%.[4−6] Other vital aspects of this technology are their low cost, compatibility with high-throughput mass manufacturing, their low weight, and color tunability.[3,7] To date, most research has focused on devices on transparent substrates, i.e., a superstrate configuration. PSCs with an opaque substrate configuration, however, still fall behind with a highest reported PCE of only 15%.[8] We recently reported on a substrate PSC with an opaque Au bottom electrode and a transparent dielectric−metal−dielectric (DMD) top electrode.[9] A main limitation of this configuration is the optical loss originating from the transparent MoO_3/thin-Au/polystyrene (PS) top electrode and the thick (260 nm) doped 2,2′,7,7′-tetrakis[*N*,*N*-di(4-methoxyphenyl)amino]-9,9′-spirobifluorene (spiro-OMeTAD) hole transport layer (HTL). The elimination of these optical losses is imperative for more efficient devices.

The parasitic absorption by the thick doped spiro-OMeTAD HTL is a common denominator in many studies for top-illuminated semitransparent and substrate-configuration PSCs.[10−16] The most successful strategy to resolve this issue is to replace the solution processed doped spiro-OMeTAD HTL with a thinner, less-absorbing HTL.[17−19] Raiford et al. successfully replaced doped spiro-OMeTAD with a thin evaporated pristine 2,2′,7,7′-tetra(*N*,*N*-di-*p*-tolyl)amino-9,9-bifluorene (spiro-TTB)/atomic layer deposited VO_x bilayer HTL with minimal absorption reaching 13.2% efficiency in semitransparent PSCs.[17] In another example of a semitransparent device architecture, Wang et al. demonstrated 13.3% efficient color-tunable PSCs using a solution-processed copper(I) thiocyanate (CuSCN) HTL with minimal absorption.[19] For substrate-configuration PSCs, Heo et al. achieved 15% efficient devices with a thin poly[bis(4-phenyl)(2,4,6-

Received: October 26, 2020
Accepted: March 3, 2021
Published: March 12, 2021

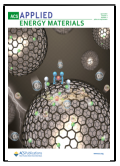

trimethylphenyl)amine] (PTAA) HTL using an anodized Ti foil bottom electrode and a laminated graphene polydimethylsiloxane transparent top electrode.[8] Although the reduction of the parasitic optical losses have been extensively studied for semitransparent devices, the vast majority of studies for substrate-configuration PSCs on opaque substrates have employed doped spiro-OMeTAD as the HTL.

Herein, we investigate replacing doped spiro-OMeTAD with a thin thermally evaporated organic HTL in a substrate-configuration PSC using a thick Au bottom electrode and a DMD transparent top electrode. Thin thermally evaporated HTLs such as *N*,*N*′-di(1-naphthyl)-*N*,*N*′-diphenyl-(1,1′-biphenyl)-4,4′-diamine) (NPB) and tris(4-carbazoyl-9-ylphenyl)amine) (TCTA) have been used successfully before in p−i−n PSCs.[20,21] We start from a semitransparent n−i−p PSC in which a perovskite layer is sandwiched between a transparent indium tin oxide (ITO) bottom electrode with a [6,6]-phenyl-C_{61}-butyric acid methyl ester (PCBM) passivated SnO_2 electron transport layer (ETL) and top contact consisting of a doped spiro-OMeTAD HTL and a MoO_3/thin-Au transparent electrode. To select the optimal HTL, we first fabricated semitransparent PSCs with different thicknesses of thermally evaporated and undoped spiro-OMeTAD, NPB, or TCTA as HTL. Next, using optical simulations, we optimized the DMD top electrode in the semitransparent PSC by selecting an optimal top dielectric. Finally, we transferred the semitransparent PSC stack onto an opaque Au bottom electrode which was deposited on a smooth ITO glass substrate. The best substrate PSC with the optimized thin HTL and DMD achieves a stabilized PCE of 13.1% compared to 14.0% for the best substrate configuration device with a thick doped spiro-OMeTAD HTL. The lower efficiency of substrate PSCs with the thin HTL is due to a reduced open-circuit voltage (V_{oc}) and fill factor (FF), despite a higher short-circuit current density (J_{sc}). Optical modeling shows that the absorption of the thin evaporated HTL layer is negligible and that the remaining optical losses of this stack are caused by reflection of light from the top dielectric and absorption by the thin Au layer in the DMD.

2. EXPERIMENTAL SECTION

2.1. Materials and Solution Preparation. All materials and reagents were purchased from commercial sources. Solutions were stirred at 60 °C overnight before the spin coating, unless stated otherwise. For the ETL, a commercial 15 wt % SnO_2 aqueous colloidal dispersion (Alfa Aesar) was used without dilution. The dispersion was stirred overnight at room temperature. [6,6]-Phenyl-C_{61}-butyric acid methyl ester (PCBM) (Solenne BV, 99%) was dissolved in chlorobenzene (CB) (Sigma-Aldrich, anhydrous 99.8%) at a concentration of 10 mg mL^{-1}. For the perovskite precursor solution, PbI_2 (553 mg) (TCI Chemicals, 99.99% trace metal basis) was dissolved in a mixture of dimethylformamide (0.876 mL) (DMF, Sigma-Aldrich, anhydrous 99.8%) and dimethyl sulfoxide (DMSO, 0.0864 mL) (Sigma-Aldrich, anhydrous 99.9%). Formamidinium iodide (54.0 mg) (FAI, Greatcell Solar), methylammonium iodide (14.3 mg) (MAI, Greatcell Solar), and methylammonium bromide (7.6 mg) (MABr, Greatcell Solar) were dissolved in 2-propanol (1 mL) (Sigma-Aldrich, anhydrous 99.5%). As evaporated pristine HTLs, spiro-OMeTAD (Lumtec, 99.5%), *N*,*N*′-di(1-naphthyl)-*N*,*N*′-diphenyl-(1,1′-biphenyl)-4,4′-diamine) (NPB, Lumtec, 99%), and tris(4-carbazoyl-9-ylphenyl)amine) (TCTA, Lumtec, 99%) were used. For the thermally evaporated top dielectric, ZnS (Alfa Aesar, 99.995% (metals basis)) was used.

2.2. Device Fabrication. All thermally evaporated films were deposited under high-vacuum conditions at ∼5 × 10^{-7} mbar. Prepatterned ITO (110 nm) glass substrates (Naranjo Substrates) were cleaned in the following sequence: sonication in acetone (15 min), scrubbing and sonication in sodium dodecyl sulfate solution (Acros, 99%) in water (10 min), rinsing in deionized water, and sonication in 2-propanol (15 min). Prior to device preparation the substrates were blow-dried with nitrogen and further cleaned by UV-ozone (30 min). For the Au-based substrate-configuration devices a 120 nm patterned Au bottom electrode was deposited (1 Å s^{-1}) onto the ITO glass substrate via thermal evaporation. On top of the Au bottom electrode, a 10 nm full area substoichiometric MoO_3 (Sigma-Aldrich, 99.9%) interlayer was deposited (0.5 Å s^{-1}) via thermal evaporation. The SnO_2 dispersion was spin-coated onto the ITO substrate, or onto the MoO_3-coated substrate for Au-based cells at 2800 rpm (with a 2000 rpm s^{-1} acceleration) for 60 s and heat-treated at 150 °C for 30 min in an ambient atmosphere. The SnO_2 (85 nm) film was then treated with UV-ozone (10 min) and immediately transferred into a nitrogen-filled glovebox. To passivate the SnO_2 ETL, the PCBM solution was spin-coated onto the SnO_2 coated substrate at 2000 rpm (with a 2000 rpm s^{-1} acceleration) for 30 s and annealed at 100 °C (30 min) to leave an ∼1 nm PCBM passivation layer. After annealing the substrates were cooled to room temperature. The $FA_{0.66}MA_{0.34}PbI_{2.85}Br_{0.15}$ perovskite film (445 nm) was processed onto the PCBM passivated substrate by using two spin-coating steps at 3000 rpm (with a 2000 rpm s^{-1} acceleration) for 60 s. First, the PbI_2 solution was statically spin-coated onto the PCBM passivated substrate, followed by the dynamic spin-coating of the FAI/MAI/MABr solution 30 s before the end of the program. Prior to depositing the HTL, the sample was annealed in the glovebox at 100 °C for 30 min and cooled to room temperature. Thermally evaporated pristine spiro-OMeTAD, NPB, and TCTA HTLs were deposited (2 Å s^{-1}) onto the $FA_{0.66}MA_{0.34}PbI_{2.85}Br_{0.15}$ perovskite film. Next, a 15 nm full area MoO_3 film and a 7 nm patterned Au top electrode were deposited (0.5 Å s^{-1} both) via thermal evaporation. To finalize the DMD stack, the ZnS top dielectric was deposited (0.5 Å s^{-1}) onto the Au top electrode via thermal evaporation. The active area (0.09 or 0.16 cm^2) was determined by the overlap of the ITO or Au bottom electrode and the transparent top Au electrode.

2.3. Device Characterization. All samples were stored and measured in a nitrogen-filled glovebox without any further exposure to air or any preconditioning, unless stated otherwise. The current density−voltage (*J*−*V*) characteristics were measured by a Keithley 2400 source meter. During the *J*−*V* measurements light from a tungsten−halogen lamp was filtered by a Schott GG385 UV filter and a Hoya LB120 daylight filter to mimic the AM1.5G spectrum (100 mW cm^{-2}). For bottom (ITO side) illumination of solar cells, a black shadow mask with an aperture area of 0.0676 or 0.1296 cm^2 was employed to define the illuminated cell area. For the devices with top (DMD side) illumination the illuminated cell area was 0.09 or 0.16 cm^2. During the fast *J*−*V* sweep measurements, the source meter swept the voltage either from +1.5 to −0.5 V (reverse scan) or from −0.5 to +1.5 V (forward scan) at a scan rate of 0.25 V s^{-1}. Light soaking preconditioning of the solar cells was performed by exposing the cell area to continuous illumination of simulated AM1.5G (100 mW cm^{-2}) light for a given time, followed by a fast sweep measurement. For the stabilized *J*−*V* measurement (slow sweep measurements), the open-circuit voltage (V_{oc}) of the solar cell was first tracked for 5 min under constant illumination, and then a reverse sweep from V_{oc} +0.04 to −0.04 V was performed with a step size of 0.04 V; the acquisition time of the current density at each voltage step was 5 s.

External quantum efficiency (EQE) measurements were performed in a nitrogen atmosphere. The probe light was generated by a 50 W tungsten−halogen lamp (Philips Focusline), which was modulated with a mechanical chopper (Stanford Research, SR 540) before passing through a monochromator (Oriel, Cornerstone 130). The spectral response of the device was recorded as a voltage from a preamplifier (Stanford Research, SR 570) by using a lock-in amplifier (Stanford Research, SR 830) and was calibrated by a reference silicon cell. To accurately determine the short-circuit current density ($J_{sc,EQE}$), a green LED (530 nm, Thorlabs M530L3, driven by a

https://dx.doi.org/10.1021/acsaem.0c02653
ACS Appl. Energy Mater. 2021, 4, 3033−3043

DC4104 driver) was utilized as a light bias during the EQE measurement to provide the solar cell with ~1 sun equivalent illumination intensity.

2.4. Ultraviolet Photoelectron Spectroscopy (UPS). UPS measurements were performed in a multichamber ESCALAB II system using He I radiation ($E_{He\,I}$ = 21.22 eV) and a−6 V bias. The samples were deposited on glass substrates covered with ITO and transferred into the vacuum chamber directly from a N_2 atmosphere.

2.5. Optical Simulation. Optical simulations were performed by using the transfer matrix method with Setfos 5.0 (Fluxim AG). The wavelength-dependent refractive index (n) and extinction coefficient (k) determined by spectroscopic ellipsometry used for ZnS and MoO_3 are depicted in Figure S1 of the Supporting Information. For all other materials previously reported data were used.[9]

3. RESULTS AND DISCUSSION

3.1. Optical Modeling. We recently reported on an opaque-substrate PSCs consisting of a glass/ITO/thick-Au/MoO_3/SnO_2/$FA_{0.66}MA_{0.34}PbI_{2.85}Br_{0.15}$/spiro-OMeTAD/$MoO_3$/thin-Au/polystyrene cell configuration (FA is formamidinium, MA is methylammonium). In this device the photocurrent is mainly limited by parasitic absorption by the 260 nm thick doped spiro-OMeTAD layer and reflection and absorption by the DMD top contact.[9] To further increase the photocurrent of this device, the doped spiro-OMeTAD HTL and the perovskite active layer thicknesses can be optimized. Figure 1 shows the calculated maximum attainable photocurrent (J_{max}) in these devices based on optical modeling. Upon decreasing the thicknesses of the 260 nm doped spiro-OMeTAD layer and adjusting the perovskite layer thicknesses, two distinct thickness ranges for the HTL with relatively high J_{max} values appear at 110 ± 10 nm (option 2) and below 20 nm (option 1). For our experiments, we omit the second option because of difficulties in fabricating 560 nm thick perovskite layers with the two-step deposition method used. Instead, we chose to use the thinnest possible HTL (option 1 in Figure 1) where the perovskite layer thickness remains unchanged. At such thin layers, the high photocurrent predicted for a doped spiro-OMeTAD HTL is also expected for other small molecule HTLs because of their similar refractive indices and negligible parasitic absorption.

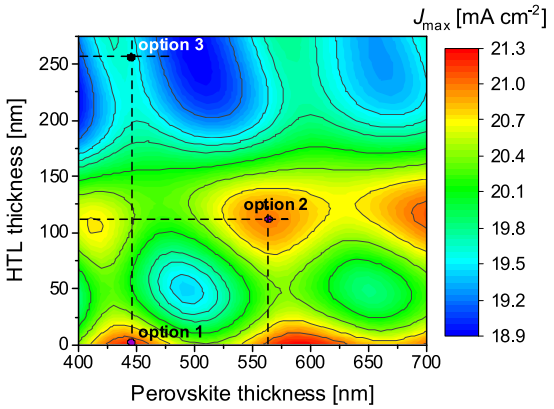

Figure 1. Simulated J_{max} as a function of the thicknesses of the doped spiro-OMeTAD HTL and the perovskite layers for an opaque-substrate PSC with top illumination. The cell configuration is glass/ITO/thick-Au/MoO_3/SnO_2/PCBM/$FA_{0.66}MA_{0.34}PbI_{2.85}Br_{0.15}$/spiro-OMeTAD/$MoO_3$/ thin-Au/top dielectric. The thicknesses of all other layers are collected in Table S1. Devices with option 3 were previously reported.[9]

For such thin layers, solution processing of doped spiro-OMeTAD films results in a poor film quality with pinholes. Instead, we use thermally evaporated pristine HTLs. Thermal evaporation provides films with precisely controlled thickness and good conformity.[22−25] When changing layer thickness of the perovskite layer and HTL, it is necessary to adapt the DMD top electrode. The steps taken in the optimization are depicted in Figure 2. As baseline, we use a semitransparent n−i−p cell with an ITO bottom electrode, a PCBM-passivated SnO_2 ETL, a two-step deposited double-cation perovskite ($FA_{0.66}MA_{0.34}PbI_{2.85}Br_{0.15}$) active layer, a doped spiro-OMeTAD HTL, and a semitransparent MoO_3/thin-Au top electrode (termed stack A). First, we tested different thermally evaporated undoped thin HTLs resulting in an updated semitransparent device stack (stack B). After optimizing the HTL thickness, we selected a suitable top dielectric to accommodate the thickness change of the HTL (stack C). As final step in the optimization, we transferred the entire stack onto an Au bottom electrode with a MoO_3 buffer layer (stack D). The subsections below describe the details of each modification. The resulting optimized thicknesses of each layer in the various configurations are listed in Table S1 of the Supporting Information.

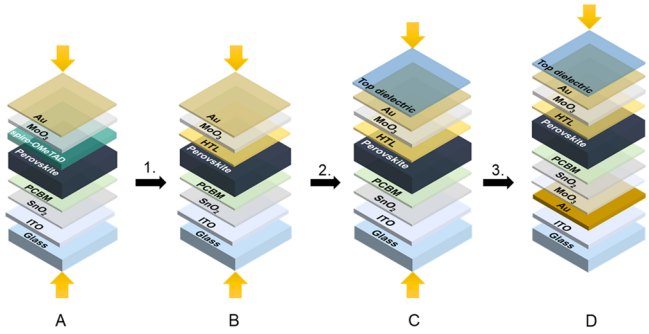

Figure 2. Stepwise optimization of a semitransparent perovskite solar cell with a thick doped spiro-OMeTAD HTL (stack A) into a substrate-configuration cell on an opaque Au bottom electrode PSC with a thin HTL and DMD top electrode (stack D).

3.2. Replacing Doped Spiro-OMeTAD in Semitransparent and Substrate-Configuration Cells. We investigated three different thermally evaporated undoped HTLs: spiro-OMeTAD, NPB, and TCTA. The flat-band energy diagram of the various layers in the semitransparent device stack determined by ultraviolet photoelectron spectroscopy (UPS) is shown in Figure 3. For doped spiro-OMeTAD we used data from the literature.[26] The UPS data of the thin HTLs deposited onto the perovskite layer are collected in Table S2 and Figure S2.

Stolterfoht et al. demonstrated that minimizing the energy offset between the highest occupied molecular orbital (HOMO) of the HTL and valence band maximum (VBM) of the perovskite is a key requirement for maximizing V_{oc}.[28] To account for the low mobility of undoped HTLs we tested varying thicknesses of HTLs with HOMO levels below (pristine spiro-OMeTAD: −5.0 eV; NPB: −5.36 eV) and above (TCTA: −5.6 eV) the HOMO of solution-processed doped spiro-OMeTAD (about −5.5 eV). The fast-scan current density−voltage (J−V) curves of semitransparent (stack B) cells illuminated through the bottom ITO electrode with

https://dx.doi.org/10.1021/acsaem.0c02653
ACS Appl. Energy Mater. 2021, 4, 3033−3043

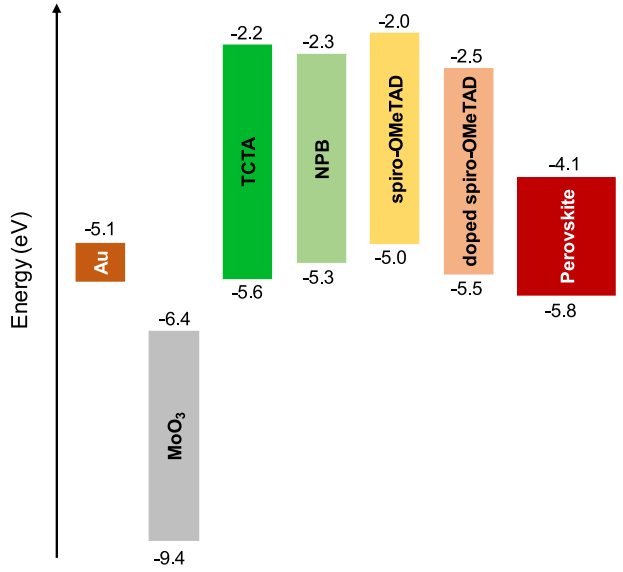

Figure 3. Flat-band energy diagram of Au, MoO_3, TCTA, NPB, spiro-OMeTAD, doped spiro-OMeTAD, and $FA_{0.66}MA_{0.34}PbI_{2.85}Br_{0.15}$ perovskite. Valence band maxima and HOMO levels were determined by UPS. Conduction band minima and LUMO levels were calculated by using the optical bandgaps and or by using the bandgap reported in the literature for MoO_3.[27]

different thicknesses and types of HTLs are summarized in Figure 4.

Varying the thickness of small molecule HTLs can dramatically impact the $J-V$ characteristics. The optimal thickness of pristine spiro-OMeTAD, NPB, and TCTA was 7.5, 10, and 7.5 nm, respectively. Devices with lower HTL thicknesses gave V_{oc}'s below 1 V. Poor performance for such devices is due to strong recombination at the HTL/perovskite interface, originating from the partial surface coverage of the HTL on the perovskite active layer or from the penetration of MoO_3 through the thin HTL. In both cases MoO_3 makes a direct contact with the perovskite, which is known to yield a poor contact that is vulnerable for interface recombination.[29,30] Semitransparent PSCs with a thicker HTL than the optimal value yielded $J-V$ characteristics with S-shape for NPB and TCTA and a reduced V_{oc} for spiro-OMeTAD. The presence of the S-shape in the $J-V$ characteristics of devices with thick undoped HTLs could be due to lower hole mobility of these films.[31,32] This behavior is related to the p-type doping of the HTL by MoO_3 at the interface of these two layers, resulting in a lower contact resistance between the HTL and Au aided by the MoO_3.[33] The doping effect of the MoO_3 only influences the first few nanometers of the HTL because the penetration of MoO_3 into a small-molecule layer occurs in a depth range of 2−3 nm,[31,34] explaining why thicker HTLs develop an S-shape.

Figure 5 compares the statistics of the device performance of PSCs with optimized evaporated thin-layer HTLs (stack B) with that of a solution-processed doped spiro-OMeTAD HTL

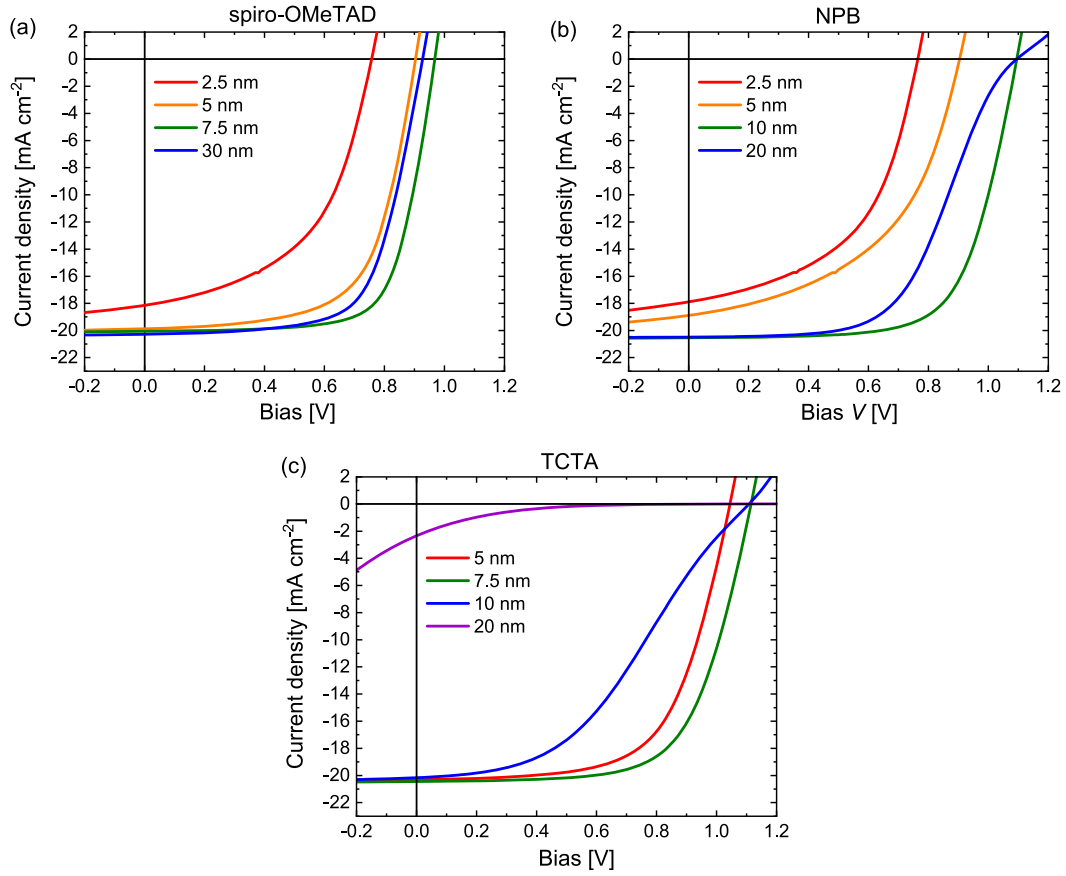

Figure 4. $J-V$ characteristics (fast scans) of semitransparent glass/ITO/SnO_2/PCBM/perovskite/thin-HTL/MoO_3/thin-Au (stack B in Figure 2) cells for different thicknesses of the evaporated pristine HTL with illumination through the bottom ITO electrode: (a) spiro-OMeTAD, (b) NPB, and (c) TCTA.

https://dx.doi.org/10.1021/acsaem.0c02653
ACS Appl. Energy Mater. 2021, 4, 3033−3043

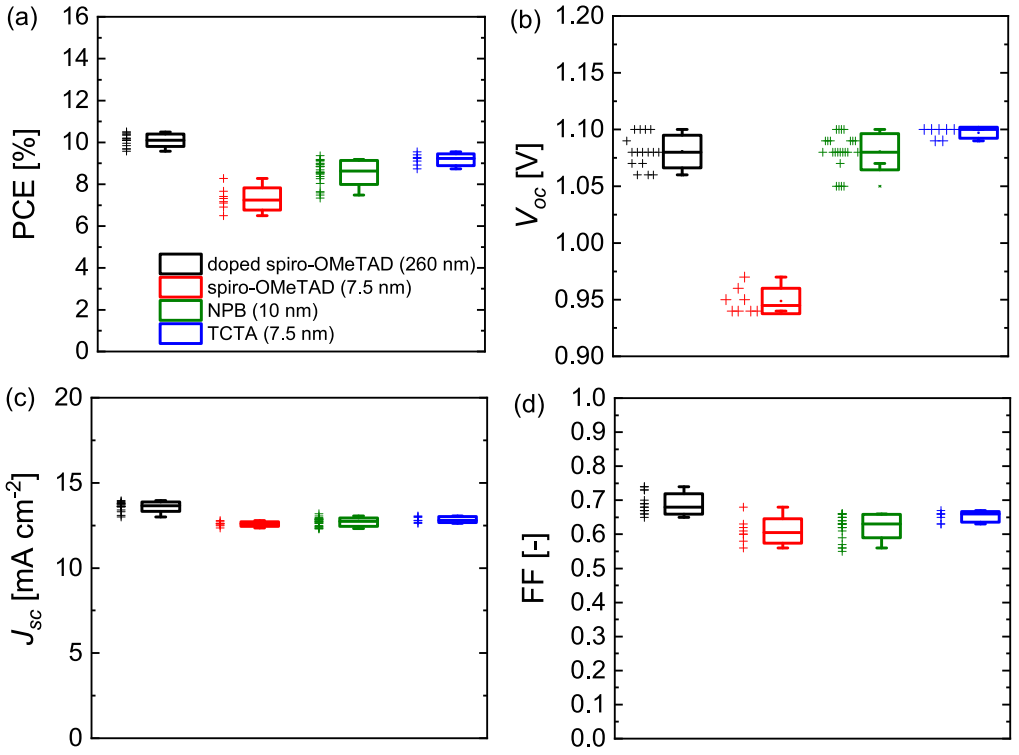

Figure 5. (a–d) Statistics and box plots of the photovoltaic parameters of optimized semitransparent glass/ITO/SnO_2/PCBM/perovskite/HTL/MoO_3/thin-Au (stack B in Figure 2) cells for three thin evaporated HTLs and a thick doped spiro-OMeTAD HTL for DM side illumination with AM.15 G light (100 mW cm^{-2}) (fast reverse scans).

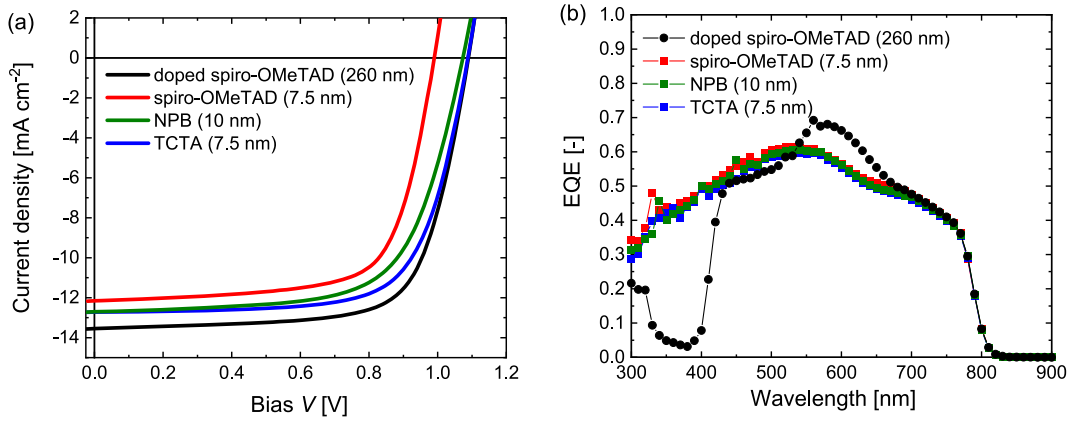

Figure 6. (a) Stabilized J–V characteristics of optimized semitransparent glass/ITO/SnO_2/PCBM/perovskite/HTL/MoO_3/thin-Au cells (stack B in Figure 2) for three thin evaporated HTLs and a thick doped spiro-OMeTAD HTL for DM side illumination with AM.15 G light (100 mW cm^{-2}). (b) Corresponding EQE spectra.

Table 1. Photovoltaic Parameters of Semitransparent Cells with a DM Top Electrode[a]

HTL (thickness)	J_{sc} [mA cm^{-2}]	$J_{sc,EQE}$ [mA cm^{-2}]	V_{oc} [V]	FF [–]	PCE [%]	PCE_{EQE} [%]
doped spiro-OMeTAD (260 nm)	13.5	13.4	1.09	0.71	10.4	10.4
spiro-OMeTAD (7.5 nm)	12.2	13.8	0.99	0.70	8.4	9.6
NPB (10 nm)	12.7	13.6	1.07	0.66	9.0	9.7
TCTA (7.5 nm)	12.7	13.4	1.09	0.70	9.7	10.1

[a]Obtained from slow reverse scan with top (DM-side) illumination.

(stack A) with illumination through the semitransparent MoO_3/Au dielectric–metal (DM) top contact. The stabilized-scan J–V characteristics of the optimized semitransparent devices are depicted in Figure 6a, and the photovoltaic parameters are collected in Table 1. Devices with evaporated HTLs exhibited low hysteresis (Table S3). Therefore, we only discuss results related to the reverse scan direction. PSCs with evaporated HTLs yielded lower average efficiencies than those with doped spiro-OMeTAD HTL. The average efficiency with top (DM side) illumination devices with thin evaporated spiro-

https://dx.doi.org/10.1021/acsaem.0c02653
ACS Appl. Energy Mater. 2021, 4, 3033–3043

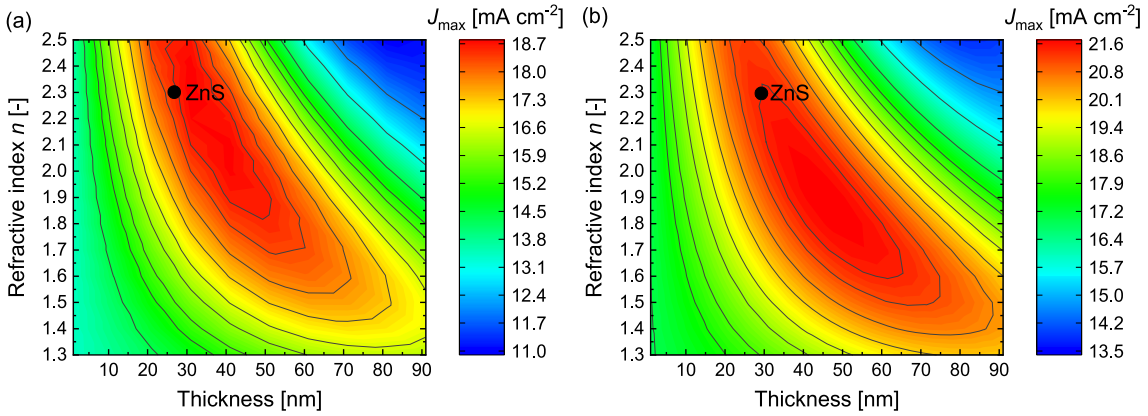

Figure 7. (a) Maximum AM1.5G photocurrent (J_{max}) for top illumination determined by optical modeling for a semitransparent glass/ITO/SnO_2/PCBM/$FA_{0.66}MA_{0.34}PbI_{2.85}Br_{0.15}$/NPB/$MoO_3$/thin-Au/top dielectric (stack C) cell as a function of the thickness and refractive index (n) of the top dielectric layer. ZnS indicates the optimal thickness for ZnS layer. (b) Same for an opaque glass/ITO/thick-Au/MoO_3/SnO_2/PCBM/$FA_{0.66}MA_{0.34}PbI_{2.85}Br_{0.15}$/NPB/$MoO_3$/thin-Au/top dielectric (stack D) cell.

OMeTAD, NPB, and TCTA HTLs was 7.3 ± 0.5%, 8.8 ± 0.4%, and 9.2 ± 0.3% compared to 10.2 ± 0.3% for a thick doped spiro-OMeTAD HTL (Figure 5). The differences among the PCEs of cells with the thin HTLs are mainly related to differences in V_{oc} (Figure 5b) and correspond to the varying offsets between the HOMO of the HTLs and the VBM of $FA_{0.66}MA_{0.34}PbI_{2.85}Br_{0.15}$ (Figure 3). The short-circuit current densities ($J_{sc,EQE}$), determined by integrating the product of the external quantum efficiency (EQE) (Figure 6b), the elementary charge, and the Air Mass 1.5 Global (AM1.5G) (100 mW cm^{-2}) spectral irradiance over all wavelengths, of the thin-HTL cells are between 13.4 and 13.8 mA cm^{-2} and comparable to 13.4 mA cm^{-2} for the cell with the thick doped spiro-OMeTAD layer (Table 1). The higher EQE values below 400 nm in the EQE spectra of the cells with a thin HTL (Figure 6b) can directly be attributed to the reduced absorption in that region.

For these semitransparent cells the photocurrent (I) increases with photon flux (Φ) at 730 nm following a power law behavior ($I \propto \Phi^{\alpha}$) with an exponent very close to unity (α = 0.98−1.00) over 3 orders of magnitude for ITO- and DM-side illumination (Figure S3 and Table S4), suggesting negligible bimolecular recombination at short circuit. The ideality factor (n) determined from the light intensity dependence of V_{oc} (illumination with 730 nm light) is slightly higher for cells with the doped spiro-OMeTAD HTL (n = 1.81 ± 0.10) than for cells with the thin pristine HTLs (n = 1.56 ± 0.07), except for the cell with pristine spiro-OMeTAD HTL (n = 1.23) when illuminated from the ITO side. Here the low V_{oc} = 0.97 V and n = 1.23 indicate appreciable surface recombination (Figure S3 and Table S4). The higher ideality factor for the doped spiro-OMeTAD suggests a higher relative contribution of the trap-assisted recombination in these cells at open circuit.

Based on $J_{sc,EQE}$, the best semitransparent PSCs with TCTA as HTL reach PCE_{EQE} = 10.1% efficiency, which is comparable to the PCE_{EQE} of 10.4% obtained for the best thick doped spiro-OMeTAD PSC (Table 1). Using J_{sc} from the solar simulator, the PCEs are 9.7% and 10.4%. The difference arises from a larger mismatch between J_{sc} and $J_{sc,EQE}$ for cells with a thin HTL (Table 1), caused by the different EQE spectra for cells with thick and thin HTLs (Figure 6b). Devices with TCTA had a limited shelf-lifetime as concluded from the noticeable discoloration of the Au top electrode and the loss of J_{sc}. Possibly, TCTA can be employed in combination with other top electrodes, but with Au the cells quickly deteriorate. The origin of the instability of the TCTA/MoO_3/Au stack on top of the perovskite layer has not been investigated. At its optimal thickness (7.5 nm) the TCTA layer might not be fully closed, causing a direct contact between MoO_3 and perovskite, which are known to react.[29,30,35] It has also been shown that the organic HTL/MoO_3 interface can be unstable, resulting in buckling an wrinkling induced by nanoscopic pores in the organic HTL.[18] The devices with evaporated pristine spiro-OMeTAD and NPB did not show any signs of Au electrode migration and reached PCE_{EQE} of 9.6% and 9.7%, respectively (Table 1). We note that the instability of the TCTA/MoO_3/Au stack is not directly related to the glass transition temperature (T_g) of the organic HTL, as T_g = 151 °C for TCTA[36] is actually higher than that of spiro-OMeTAD (T_g = 121 °C)[37] and NPB (T_g = 95 °C).[38] For further optimization, we selected a 10 nm NPB layer because of its higher V_{oc} and more reproducible performance.

The $J_{sc,EQE}$ of the devices with a MoO_3/thin-Au top electrode is strongly limited by the reflection of light. We performed optical simulations to find a suitable top dielectric to ensure optimal light incoupling into the active layer (Figure 7). The semitransparent cell with the complete dielectric−metal−dielectric top electrode is termed stack C. In the modeling we varied the thickness and the refractive index (n) of the ideal top dielectric, assuming that it has no absorption (k = 0). Figure 7a shows that the highest photocurrent of 18.7 mA cm^{-2} can be reached when n is between 1.9 and 2.5 at thicknesses ranging from 50 to 30 nm. Accordingly, a 30 nm ZnS top dielectric with $n \approx 2.3$ and k = 0 ensures optimal light incoupling. ZnS can be thermally evaporated which is less damaging for thin HTLs than a solution-processed top dielectric (e.g., polystyrene) as used previously for thick HTLs.[9] Instead of ZnS, a MoO_3 layer can be used as top dielectric. Because for MoO_3 $n \approx 2.0$ (Figure S1), the required thickness would be about 40 nm.

In a next step, semitransparent devices were fabricated with a MoO_3/thin-Au/ZnS DMD top electrode (stack C, with ZnS as top dielectric). The devices were tested with top and bottom illumination. The J−V characteristics and EQE spectra are shown in Figure 8 together with a photograph of a substrate

https://dx.doi.org/10.1021/acsaem.0c02653
ACS Appl. Energy Mater. 2021, 4, 3033−3043

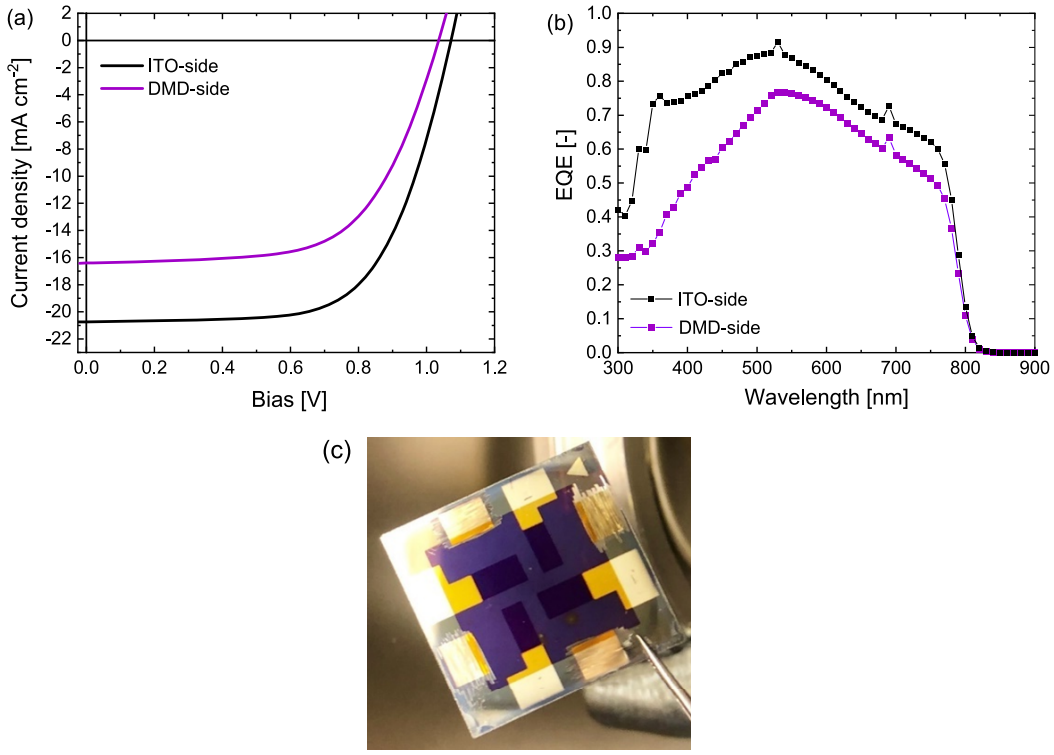

Figure 8. (a) Stabilized $J-V$ characteristics of optimized semitransparent glass/ITO/SnO_2/PCBM/$FA_{0.66}MA_{0.34}PbI_{2.85}Br_{0.15}$/NPB/$MoO_3$/thin-Au/ZnS (stack C) PSCs illuminated from ITO (black) and DMD side (purple) with simulated AM.15 G light (100 mW cm^{-2}). (b) Corresponding EQE spectra. (c) Photograph of substrate with four devices.

Table 2. Photovoltaic Parameters of Optimized Semitransparent and Opaque Cells with 10 nm NPB as the Hole Transport Layer[a]

stack[b]	illumination side	sweep type	J_{sc} [mA cm^{-2}]	$J_{sc,EQE}$ [mA cm^{-2}]	V_{oc} [V]	FF [−]	PCE [%]	PCE_{EQE} [%]
A[c]	ITO	fast	20.4	19.9	1.10	0.69	15.4	15.1
	Au/MoO_3	fast	13.6		1.10	0.66	9.8	
	Au/MoO_3	slow	13.5	13.4	1.09	0.71	10.4	10.4
B	ITO	fast	20.6	20.5	1.09	0.69	15.5	15.4
	Au/MoO_3	fast	13.2		1.08	0.66	9.4	
	Au/MoO_3	slow	12.7	13.6	1.07	0.66	9.0	9.7
C	ITO	fast	20.8	20.1	1.09	0.68	15.5	14.9
	ZnS/Au/MoO_3	fast	16.3	16.2	1.09	0.64	11.4	11.3
	ZnS/Au/MoO_3	slow	16.4	16.6	1.04	0.62	10.5	10.7
D	ZnS/Au/MoO_3	fast	17.9		1.06	0.67	12.6	
	ZnS/Au/MoO_3	slow	18.2	18.3	1.07	0.67	13.1	13.1

[a] $J-V$ characteristics were obtained in reverse scans. [b] See Figure 2 for stack configurations. [c] Using a 260 nm doped spiro-OMeTAD instead of a thin NPB HTL.

with four cells. The relevant $J-V$ parameters are summarized in Table 2. The average $J-V$ parameters for illumination from both sides indicate negligible hysteresis (Table S5). The best semitransparent cells with a DMD top contact achieved 14.9% efficiency when illuminated from the ITO side and 10.7% from the DMD side (Table 2). The average V_{oc} and FF for both illumination directions were rather similar, and the difference in PCE was mainly caused by their different $J_{sc,EQE}$ (Table S5). The lower $J_{sc,EQE}$ of a top-illuminated cell is related to optical losses originating from the DMD top electrode. The difference in $J_{sc,EQE}$ between top and bottom illumination of these optimized semitransparent cells equals 3.5 mA cm^{-2} by using the thin NPB layer as HTL (Table 2, stack C) compared to a 4.3 mA cm^{-2} when using a thick doped spiro-OMeTAD HTL.[9] The lower $J_{sc,EQE}$ difference for the NPB cell stems from the reduced parasitic absorption. This is supported by the reduced losses in the EQE spectrum between 300 and 400 nm for cells that use a thin NPB HTL (Figure 8b). The corresponding differences in J_{sc} determined from the $J-V$ data by using the solar simulator point in the same direction but are slightly larger: 4.4 mA cm^{-2} for thin NPB (Table 2, stack C) and 4.8 mA cm^{-2} for thick doped spiro-OMeTAD.[9]

In the last step, we transformed the semitransparent cells into an opaque substrate device configuration (stack D). We fabricated substrate-configuration devices on glass substrates using a thick Au bottom electrode coated with a 10 nm MoO_3 layer. The interfacial MoO_3 layer serves to improve the wetting of the aqueous colloidal SnO_2 dispersion that is spin collated on top. The MoO_3/SnO_2 interface allows a barrier-free extraction of electrons.[39] The results are compared to

https://dx.doi.org/10.1021/acsaem.0c02653
ACS Appl. Energy Mater. 2021, 4, 3033−3043

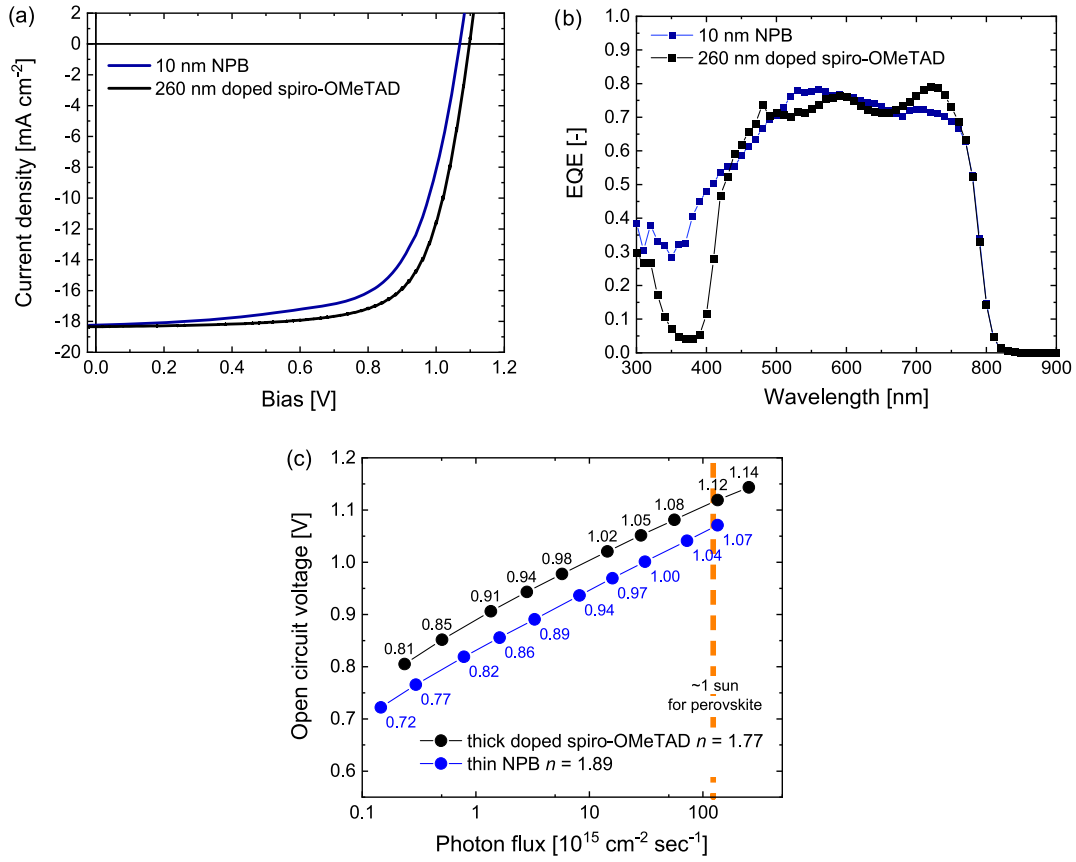

Figure 9. (a) Stabilized $J-V$ characteristics of substrate-configuration PSCs (glass/ITO/thick-Au/MoO_3/SnO_2/PCBM/$FA_{0.66}MA_{0.34}PbI_{2.85}Br_{0.15}$/HTL/$MoO_3$/thin-Au/ZnS) with simulated AM1.5G light (100 mW cm^{-2}) illumination for thin NPB and thick doped spiro-OMeTAD HTLs. (b) Corresponding EQE spectra, recorded with 530 nm bias light. (c) Photon flux dependence of V_{oc} at 730 nm.

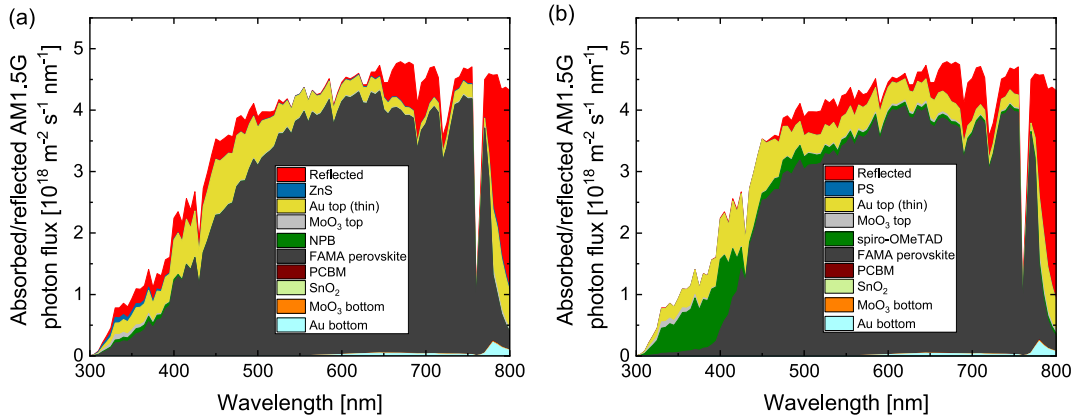

Figure 10. (a) AM1.5G photon flux reflected, transmitted, or absorbed by each individual layer in the opaque substrate−cell with a thin NPB HTL (stack D) as a function of wavelength. (b) Same for a cell with a thick doped spiro-OMeTAD HTL. The enlarged versions of (a) and (b) can be found in Figures S6 and S7, respectively.

opaque-substrate cells with a thick doped spiro-OMeTAD reported previously.[9] The optimal thickness of the top dielectric was determined by using optical simulation (Figure 7b). A J_{max} of 21.6 mA cm^{-2} can be expected for a refractive index between 1.7 and 2.2 and a thickness in the range between and 60 and 35 nm (Figure 7b). For the opaque (stack D) devices we thus used a 30 nm thin ZnS ($n \sim 2.3$) top dielectric, the same as for semitransparent (stack C) cells. This gives a theoretical J_{max} of 21.0 mA cm^{-2}.

The stabilized $J-V$ characteristics, EQE plots, and intensity dependence of V_{oc} of an opaque substrate-configuration PSC with a thin NPB layer (stack D) cells are shown in Figure 9 and compared to those using a thick spiro-OMeTAD HTL. The corresponding $J-V$ parameters are summarized in Table 2. The average reverse and forward fast sweep $J-V$ characteristics for both stacks are summarized in Table S5. The opaque substrate-configuration PSCs require light soaking to achieve their best performance (Figure S4 and Table S6). Thermally evaporated MoO_3 is substoichiometric, and illumination causes formation of color centers that enhance the electrical conductivity and reduce series resistance.[40]

https://dx.doi.org/10.1021/acsaem.0c02653
ACS Appl. Energy Mater. 2021, 4, 3033−3043

Table 3. $q\Phi$ Reflected, Transmitted, or Absorbed by Each Layer in Opaque-Substrate PSCs[a]

	NPB		doped spiro-OMeTAD	
layer	thickness [nm]	$q\Phi$ [mA cm^{-2}]	thickness [nm]	$q\Phi$ [mA cm^{-2}]
air (reflected)	∞	1.7	∞	1.7
ZnS/PS	30	0.1	50	∼0
Au top (thin)	7	2.7	7	2.7
MoO_3	15	0.2	15	0.2
NPB/spiro-OMeTAD	10	0.1	260	1.6
$FA_{0.66}MA_{0.34}PbI_{2.85}Br_{0.15}$	445	21.0	445	19.5
PCBM	1	∼0	1	∼0
SnO_2	85	∼0	85	∼0
MoO_3	10	∼0	10	∼0
Au bottom	120	0.1	120	0.2
air (transmitted)	∞	∼0	∞	∼ 0

[a]Integration from 300 to 775 nm, for all layers except for the perovskite layer where integration was up to 800 nm.

The optimized opaque substrate-configuration PSC with a thin NPB HTL (stack D) cell achieves a stabilized PCE_{EQE} of 13.1% (Table 2). This performance is slightly lower than the PCE_{EQE} of 14.0% for the cell that uses a thick doped spiro-OMeTAD.[9] The lower efficiency for the NPB cell is due to a lower V_{oc} (1.07 vs 1.10 V) and FF (0.67 vs 0.70) despite an increased $J_{sc,EQE}$ (18.3 vs 17.9 mA cm^{-2}). Compared to a thick doped spiro-OMeTAD, the cells that use a thin-NPB layer show an improved EQE in the 300−430 and 500−580 nm spectral ranges but a loss for 670−760 nm wavelengths (Figure 9b). This loss is unexpected from optical simulations (Figure S5) and is tentatively ascribed to a different perovskite thickness or surface roughness. The $J_{sc,EQE}$ of 18.3 mA cm^{-2} results in an estimated internal quantum efficiency (IQE) of 87% when compared to the J_{max} of 21.0 mA cm^{-2} obtained from optical modeling. This value is lower than the IQE of 92% found for cells with a thick doped spiro-OMeTAD layer[9] and rationalizes the moderate increase in photocurrent. To investigate charge recombination, we recorded the V_{oc} as a function of photon flux (Figure 9c). From the slope in the semilogarithmic plot an ideality factor n = 1.89 was estimated for the cell with the thin NPB layer, slightly higher than n = 1.77 for the cell with the thick-doped spiro-OMeTAD HTL. The high ideality factors for both cells suggests a significant contribution of trap-assisted recombination. The overall lower performance of the cells with a thin-NPB layer may be related to insufficient doping of NPB by MoO_3.[41]

3.3. Optical Loss Analysis of Substrate Cells. The optical losses of the opaque-substrate PSC with a thin NPB HTL (stack D) was quantified by using simulations. The wavelength-dependent optical loss is visualized by the product of the absorptance or reflectance of each layer and the AM1.5 G photon flux (Figure 10). Table 3 lists the product of the elementary charge q [C] and the AM.15G photon flux density Φ [# photons cm^{-2} s^{-1}] integrated over the spectral range of the cell that is reflected, transmitted, or absorbed by each layer in the cells with either a thin NPB layer or a thick doped spiro-OMeTAD HTL. For the perovskite layer the $q\Phi$ product corresponds to the maximum generated photocurrent [mA cm^{-2}].

The total optical photocurrent loss was estimated from wavelengths between 300 and 775 nm which add up to 4.9 mA cm^{-2} for the NPB cell (stack D) as compared to 6.4 mA cm^{-2} for the spiro-OMeTAD cell. We choose the arbitrary upper limit of 775 nm as it is slightly lower than the bandgap and avoids overestimating reflectance and transmittance losses. The major optical losses of the substrate-configuration cell with the thin-NPB layer (stack D) is due to the absorption of the thin-Au top electrode (2.7 mA cm^{-2}, yellow area in Figure 10a) and due to the reflection from the top dielectric (1.7 mA cm^{-2}, red area in Figure 10a). In the EQE spectra of top illuminated substrate-configuration (stack D) cells reduced optical losses were observed between 300 and 400 nm for cells by using a thin NPB layer compared to cells with a thick doped spiro-OMeTAD layer (Figure 9b). Based on optical modeling, the higher $J_{sc,EQE}$ values of these devices are due to the reduced absorption of the NPB HTL (0.1 mA cm^{-2}, green area in Figure 10a) which is significantly less than 1.6 mA cm^{-2} for substrate-configuration cells with a thick doped spiro-OMeTAD (green area in Figure 10b). Optical losses originating from the ZnS and MoO_3 only amount to 0.3 mA cm^{-2}. The optical losses in SnO_2, PCBM, and Au are limited to 0.1 mA cm^{-2} because of the strong absorption by the thick perovskite active layer. The theoretical photocurrent generated by absorption of light in the perovskite active layer is 21.0 mA cm^{-2} with the thin NPB layer compared to 19.5 mA cm^{-2} for the cell using a thick doped spiro-OMeTAD. We estimate an IQE value of 87% for the thin-NPB cell which is slightly lower than the IQE of 92% found for the thick spiro-OMeTAD cell. The difference between the two values is on the order of the expected accuracy of the experimental and modeling procedures. The results show that by using a thin evaporated HTL the parasitic absorption of the HTL in substrate-configuration PSCs can be almost completely eliminated.

4. CONCLUSIONS

In conclusion, we developed substrate-configuration PSCs with thin thermally evaporated pristine organic HTLs and a DMD transparent top electrode consisting of MoO_3/thin-Au/ZnS. The optimal thickness for the HTLs is 7−10 nm. Thinner layers cause a voltage loss, and thicker layers give rise to FF or V_{oc} losses. The best initial performance was obtained with TCTA, but the cells had a limited shelf lifetime due to migration of Au. Devices with NPB appeared more stable and gave only slightly lower PCEs. Based on optical modeling, a 30 nm ZnS dielectric was selected to minimize reflection of the top electrode. The optimized semitransparent PSCs gave PCEs of 10.7% for DMD-side and 14.9% for ITO-side illumination. Opaque-substrate PSCs with a thick Au bottom electrode and a MoO_3 interlayer reached 13.1% efficiency. This is somewhat lower than the best substrate-configuration device with 14.0% efficiency described recently.[9] The $J_{sc,EQE}$ of opaque cells with a

https://dx.doi.org/10.1021/acsaem.0c02653
ACS Appl. Energy Mater. 2021, 4, 3033−3043

thin undoped NPB HTL (18.3 mA cm^{-2}) is higher than that of cells with a thick doped spiro-OMeTAD HTL (17.9 mA cm^{-2}). Optical modeling suggests that the difference in photocurrent between the two configurations could even amount to 1.5 mA cm^{-2}. The fact that despite the higher photocurrent the thin HTL cells do not perform better than the thick HTL cells is due to a combination of a slightly lower IQE (87% vs 92%), V_{oc} (1.07 vs 1.10 V), and FF (0.67 vs 0.70). In the optimized cell the current density loss attributed to parasitic absorption by the NPB is only 0.1 mA cm^{-2} compared to 1.6 mA cm^{-2} for doped spiro-OMeTAD. The remaining optical losses of substrate-configuration PSC are due to the reflection from the top dielectric (1.7 mA cm^{-2}) and the absorption in the transparent Au top electrode (2.7 mA cm^{-2}).

Future experiments on a thin evaporated organic HTLs in substrate-configuration PSCs should focus on assessing (long-term) stability. An issue of possible concern is the (thermal) instability of the organic HTL/MoO_3 interface as identified by Sellinger et al.[18] and as found in this work for the TCTA/MoO_3 interface. Possibly organic HTLs with high glass transition temperatures can be beneficial in this respect.[37,38] Alternatively, pinhole-free spin-coated hole transporting polymer layers can possibly be used provided they have low optical absorption in the relevant spectral range and can be made sufficiently thin.[42] Further optimization of substrate-configuration PSCs can also focus on reducing the V_{oc} and FF losses and further enhancing incoupling of light.

■ ASSOCIATED CONTENT

Supporting Information

The Supporting Information is available free of charge at https://pubs.acs.org/doi/10.1021/acsaem.0c02653.

Additional data on optical constants, layer thickness, energy levels, device statistics, and light intensity dependence (PDF)

■ AUTHOR INFORMATION

Corresponding Author

René A. J. Janssen − *Molecular Materials and Nanosystems & Institute for Complex Molecular Systems, Eindhoven University of Technology, 5600 MB Eindhoven, The Netherlands; Dutch Institute for Fundamental Energy Research, 5612 AJ Eindhoven, The Netherlands;* orcid.org/0000-0002-1920-5124; Email: r.a.j.janssen@tue.nl

Authors

Benjamin T. Feleki − *Molecular Materials and Nanosystems & Institute for Complex Molecular Systems, Eindhoven University of Technology, 5600 MB Eindhoven, The Netherlands*

Christ H. L. Weijtens − *Molecular Materials and Nanosystems & Institute for Complex Molecular Systems, Eindhoven University of Technology, 5600 MB Eindhoven, The Netherlands*

Martijn M. Wienk − *Molecular Materials and Nanosystems & Institute for Complex Molecular Systems, Eindhoven University of Technology, 5600 MB Eindhoven, The Netherlands*

Complete contact information is available at: https://pubs.acs.org/10.1021/acsaem.0c02653

Notes

The authors declare no competing financial interest.

■ ACKNOWLEDGMENTS

We thank Tom van der Pol for determining the optical constants. This research was performed under Project F71.4.15562b in the framework of the Partnership Program of the Materials innovation institute M2i (www.m2i.nl) and the Foundation of Fundamental Research on Matter (FOM) (www.fom.nl), which is part of The Netherlands Organization for Scientific Research (www.nwo.nl). The research also received funding from the NWO Spinoza grant awarded to R.A.J.J. We further acknowledge funding from the Ministry of Education, Culture and Science (Gravity program 024.001.035).

■ REFERENCES

(1) James, T.; Goodrich, A.; Woodhouse, M.; Margolis, R.; Ong, S. *Building-Integrated Photovoltaics (BIPV) in the Residential Sector: An Analysis of Installed Rooftop System Price*; National Renewable Energy Laboratory: Golden, CO, 2011.

(2) Pagliaro, M.; Ciriminna, R.; Palmisano, G. BIPV: Merging the Photovoltaic with the Construction Industry. *Prog. Photovoltaics* **2010**, *18*, 61−72.

(3) Wojciechowski, K.; Forgács, D.; Rivera, T. Industrial Opportunities and Challenges for Perovskite Photovoltaic Technology. *Sol. RRL* **2019**, *3*, 1900144.

(4) Green, M. A.; Dunlop, E. D.; Hohl-Ebinger, J.; Yoshita, M.; Kopidakis, N.; Ho-Baillie, A. W. Y. Solar Cell Efficiency Tables (Version 55). *Prog. Photovoltaics* **2020**, *28*, 3−15.

(5) Shi, L.; Bucknall, M. P.; Young, T. L.; Zhang, M.; Hu, L.; Bing, J.; Lee, D. S.; Kim, J.; Wu, T.; Takamure, N.; McKenzie, D. R.; Huang, S.; Green, M. A.; Ho-Baillie, A. W. Y. Gas Chromatography−Mass Spectrometry Analyses of Encapsulated Stable Perovskite Solar Cells. *Science* **2020**, *368*, eaba2412.

(6) Batmunkh, M.; Zhong, Y. L.; Zhao, H. Recent Advances in Perovskite-Based Building-Integrated Photovoltaics. *Adv. Mater.* **2020**, *32*, 2000631.

(7) Extance, A. The Reality Behind Solar Power's Next Star Material. *Nature* **2019**, *570*, 429−432.

(8) Heo, J. H.; Shin, D. H.; Lee, M. L.; Kang, M. G.; Im, S. H. Efficient Organic−Inorganic Hybrid Flexible Perovskite Solar Cells Prepared by Lamination of Polytriarylamine/$CH_3NH_3PbI_3$/Anodized Ti Metal Substrate and Graphene/PDMS Transparent Electrode Substrate. *ACS Appl. Mater. Interfaces* **2018**, *10*, 31413−31421.

(9) Feleki, B. T.; Chandrashekar, S.; Bouwer, R. K. M.; Wienk, M. M.; Janssen, R. A.J. Development of a Perovskite Solar Cell Architecture for Opaque Substrates. *Sol. RRL* **2020**, *4*, 2000385.

(10) Werner, J.; Dubuis, G.; Walter, A.; Löper, P.; Moon, S. J.; Nicolay, S.; Morales-Masis, M.; De Wolf, S.; Niesen, B.; Ballif, C. Sputtered Rear Electrode with Broadband Transparency for Perovskite Solar Cells. *Sol. Energy Mater. Sol. Cells* **2015**, *141*, 407−413.

(11) Werner, J.; Weng, C. H.; Walter, A.; Fesquet, L.; Seif, J. P.; De Wolf, S.; Niesen, B.; Ballif, C. Efficient Monolithic Perovskite/Silicon Tandem Solar Cell with Cell Area > 1 cm^2. *J. Phys. Chem. Lett.* **2016**, *7*, 161−166.

(12) Werner, J.; Niesen, B.; Ballif, C. Perovskite/Silicon Tandem Solar Cells: Marriage of Convenience or True Love Story? − An Overview. *Adv. Mater. Interfaces* **2018**, *5*, 1700731.

(13) Wang, X.; Li, Z.; Xu, W.; Kulkarni, S. A.; Batabyal, S. K.; Zhang, S.; Cao, A.; Wong, L. H. Tio_2 Nanotube Arrays Based Flexible Perovskite Solar Cells with Transparent Carbon Nanotube Electrode. *Nano Energy* **2015**, *11*, 728−735.

(14) Troughton, J.; Bryant, D.; Wojciechowski, K.; Carnie, M. J.; Snaith, H.; Worsley, D. A.; Watson, T. M. Highly Efficient, Flexible, Indium-Free Perovskite Solar Cells Employing Metallic Substrates. *J. Mater. Chem. A* **2015**, *3*, 9141−9145.

(15) Han, G. S.; Lee, S.; Duff, M.; Qin, F.; Lee, J.-K. Highly Bendable Flexible Perovskite Solar Cells on a Nanoscale Surface Oxide Layer of Titanium Metal Plates. *ACS Appl. Mater. Interfaces* **2018**, *10*, 4697−4704.
(16) Han, G. S.; Lee, S.; Duff, M. L.; Qin, F.; Jiang, M.; Li, G.; Lee, J.-K. Multi-Functional Transparent Electrode for Reliable Flexible Perovskite Solar Cells. *J. Power Sources* **2019**, *435*, 226768.
(17) Raiford, J. A.; Belisle, R. A.; Bush, K. A.; Prasanna, R.; Palmstrom, A. F.; McGehee, M. D.; Bent, S. F. Atomic Layer Deposition of Vanadium Oxide to Reduce Parasitic Absorption and Improve Stability in n−i−p Perovskite Solar Cells for Tandems. *Sustain. Energy Fuels* **2019**, *3*, 1517−1525.
(18) Schloemer, T. H.; Raiford, J. A.; Gehan, T. S.; Moot, T.; Nanayakkara, S.; Harvey, S. P.; Bramante, R. C.; Dunfield, S.; Louks, A. E.; Maughan, A. E.; Bliss, L.; McGehee, M. D.; van Hest, M. F. A. M.; Reese, M. O.; Bent, S. F.; Berry, J. J.; Luther, J. M.; Sellinger, A. The Molybdenum Oxide Interface Limits the High-Temperature Operational Stability of Unencapsulated Perovskite Solar Cells. *ACS Energy Lett.* **2020**, *5*, 2349−2360.
(19) Wang, H.; Dewi, H. A.; Koh, T. M.; Bruno, A.; Mhaisalkar, S.; Mathews, N. Bifacial, Color-Tunable Semitransparent Perovskite Solar Cells for Building-Integrated Photovoltaics. *ACS Appl. Mater. Interfaces* **2020**, *12*, 484−493.
(20) Kim, B.-S.; Kim, T.-M.; Choi, M.-S.; Shim, H.-S.; Kim, J.-J. Fully Vacuum−Processed Perovskite Solar Cells with High Open Circuit Voltage Using MoO_3/NPB as Hole Extraction Layers. *Org. Electron.* **2015**, *17*, 102−106.
(21) Dänekamp, B.; Droseros, N.; Tsokkou, D.; Brehm, V.; Boix, P. P.; Sessolo, M.; Banerji, N.; Bolink, H. J. Influence of Hole Transport Material Ionization Energy on the Performance of Perovskite Solar Cells. *J. Mater. Chem. C* **2019**, *7*, 523−527.
(22) Juarez-Perez, E. J.; Leyden, M. R.; Wang, S.; Ono, L. K.; Hawash, Z.; Qi, Y. Role of the Dopants on the Morphological and Transport Properties of Spiro-MeOTAD Hole Transport Layer. *Chem. Mater.* **2016**, *28*, 5702−5709.
(23) Ono, L. K.; Schulz, P.; Endres, J. J.; Nikiforov, G. O.; Kato, Y.; Kahn, A.; Qi, Y. Air-Exposure-Induced Gas-Molecule Incorporation into Spiro-MeOTAD Films. *J. Phys. Chem. Lett.* **2014**, *5*, 1374−1379.
(24) Jung, M. C.; Raga, S. R.; Ono, L. K.; Qi, Y. Substantial Improvement of Perovskite Solar Cells Stability by Pinhole-Free Hole Transport Layer with Doping Engineering. *Sci. Rep.* **2015**, *5*, 9863.
(25) Leijtens, T.; Giovenzana, T.; Habisreutinger, S. N.; Tinkham, J. S.; Noel, N. K.; Kamino, B. A.; Sadoughi, G.; Sellinger, A.; Snaith, H. J. Hydrophobic Organic Hole Transporters for Improved Moisture Resistance in Metal Halide Perovskite Solar Cells. *ACS Appl. Mater. Interfaces* **2016**, *8*, 5981−1589.
(26) Noh, J. H.; Jeon, N. J.; Choi, Y. C.; Nazeeruddin, M. K.; Grätzel, M.; Il Seok, S. Nanostructured TiO_2/$CH_3NH_3PbI_3$ Heterojunction Solar Cells Employing Spiro-OMeTAD/Co-Complex as Hole-Transporting Material. *J. Mater. Chem. A* **2013**, *1*, 11842−11847.
(27) Meyer, J.; Kidambi, P. R.; Bayer, B. C.; Weijtens, C.; Kuhn, A.; Centeno, A.; Pesquera, A.; Zurutuza, A.; Robertson, J.; Hofmann, S. Metal Oxide Induced Charge Transfer Doping and Band Alignment of Graphene Electrodes for Efficient Organic Light Emitting Diodes. *Sci. Rep.* **2015**, *4*, 5380.
(28) Stolterfoht, M.; Caprioglio, P.; Wolff, C. M.; Márquez, J. A.; Nordmann, J.; Zhang, S.; Rothhardt, D.; Hörmann, U.; Amir, Y.; Redinger, A.; Kegelmann, L.; Zu, F.; Albrecht, S.; Koch, N.; Kirchartz, T.; Saliba, M.; Unold, T.; Neher, D. The Impact of Energy Alignment and Interfacial Recombination on the Internal and External Open-Circuit Voltage of Perovskite Solar Cells. *Energy Environ. Sci.* **2019**, *12*, 2778−2788.
(29) Schulz, P.; Tiepelt, J. O.; Christians, J. A.; Levine, I.; Edri, E.; Sanehira, E. M.; Hodes, G.; Cahen, D.; Kahn, A. High-Work-Function Molybdenum Oxide Hole Extraction Contacts in Hybrid Organic−Inorganic Perovskite Solar Cells. *ACS Appl. Mater. Interfaces* **2016**, *8*, 31491−31499.
(30) Liu, P.; Liu, X.; Lyu, L.; Xie, H.; Zhang, H.; Niu, D.; Huang, H.; Bi, C.; Xiao, Z.; Huang, J.; Gao, Y. Interfacial Electronic Structure at the $CH_3NH_3PbI_3$/MoO_x Interface. *Appl. Phys. Lett.* **2015**, *106*, 193903.
(31) Qiao, X.; Chen, J.; Li, X.; Ma, D. Observation of Hole Hopping via Dopant In MoO_x-Doped Organic Semiconductors: Mechanism Analysis and Application for High Performance Organic Light-Emitting Devices. *J. Appl. Phys.* **2010**, *107*, 104505.
(32) Diekmann, J.; Caprioglio, P.; Rothhardt, D.; Arvind, M.; Unold, T.; Kirchartz, T.; Neher, D.; Stolterfoht, M. Pathways Towards 30% Efficient Perovskite Solar Cells. arXiv: 1910.07422v1, 2019.
(33) Greiner, M. T.; Helander, M. G.; Tang, W.-M. Z.; Wang, Z.-B.; Qiu, J.; Lu, Z.-H. Universal Energy-Level Alignment of Molecules on Metal Oxides. *Nat. Mater.* **2012**, *11*, 76−81.
(34) White, R. T.; Thibau, E. S.; Lu, Z.-H. Interface Structure of MoO_3 on Organic Semiconductors. *Sci. Rep.* **2016**, *6*, 21109.
(35) Sanehira, E. M.; Tremolet de Villers, B. J.; Schulz, P.; Reese, M. O.; Ferrere, S.; Zhu, K.; Lin, L. Y.; Berry, J. J.; Luther, J. M. Stability Of Perovskite Solar Cells: Reduced Degradation Using MoO_x/Al for Hole Collection. *ACS Energy Lett.* **2016**, *1*, 38−45.
(36) Shirota, Y.; Okumoto, K.; Inada, H. Thermally Stable Organic Light-Emitting Diodes Using New Families of Hole-Transporting Amorphous Molecular Materials. *Synth. Met.* **2000**, *111*−*112*, 387−391.
(37) Ren, Y.; Ren, M.; Xie, X.; Wang, J.; Cai, Y.; Yuan, Y.; Zhang, J.; Wang, P. A Spiro-OMeTAD Based Semiconductor Composite with over 100 °C Glass Transition Temperature for Durable Perovskite Solar Cells. *Nano Energy* **2021**, *81*, 10565.
(38) Kwak, J.; Lyu, Y.-Y.; Noh, S.; Lee, H.; Park, M.; Choi, B.; Char, K.; Lee, C. Hole Transport Materials with High Glass Transition Temperatures for Highly Stable Organic Light-Emitting Diodes. *Thin Solid Films* **2012**, *520*, 7157−7163.
(39) Becker, T.; Trost, S.; Behrendt, A.; Shutsko, I.; Polywka, A.; Görrn, P.; Reckers, P.; Das, C.; Mayer, T.; Di Carlo Rasi, D.; Hendriks, K. H.; Wienk, M. M.; Janssen, R. A. J.; Riedl, T. All-Oxide MoO_x/SnO_x Charge Recombination Interconnects for Inverted Organic Tandem Solar Cells. *Adv. Energy Mater.* **2018**, *8*, 1702533.
(40) Colton, R. J.; Guzman, A. M.; Rabalais, J. W. Photochromism and Electrochromism in Amorphous Transition Metal Oxide Films. *Acc. Chem. Res.* **1978**, *11*, 170−176.
(41) Yu, J. C.; Sun, J.; Chandrasekaran, N.; Dunn, C. J.; Chesman, A. S. R.; Jasieniak, J. J. Semi-Transparent Perovskite Solar Cells with a Cross-Linked Hole Transport Layer. *Nano Energy* **2020**, *71*, 104635.
(42) Hou, Y.; Du, X.; Scheiner, S.; McMeekin, D. P.; Wang, Z.; Li, N.; Killian, M. S.; Chen, H.; Richter, M.; Levchuk, I.; Schrenker, N.; Spiecker, E.; Stubhan, T.; Luechinger, N. A.; Hirsch, A.; Schmuki, P.; Steinruck, H.-P.; Fink, R. H.; Halik, M.; Snaith, H. J.; Brabec, C. J. A Generic Interface to Reduce the Efficiency-Stability-Cost Gap of Perovskite Solar Cells. *Science* **2017**, *358*, 1192−1197.

https://dx.doi.org/10.1021/acsaem.0c02653
ACS Appl. Energy Mater. 2021, 4, 3033−3043